RSC Advances

RSC Publishing

PAPER

View Article Online
View Journal | View Issue

Cite this: *RSC Adv.*, 2013, **3**, 20113

Nanoscale phase domain structure and associated device performance of organic solar cells based on a diketopyrrolopyrrole polymer†

Evan L. Williams,*[a] Sergey Gorelik,*[a] InYee Phang,[a] Michel Bosman,[a] Chellappan Vijila,[a] Gomathy Sandhya Subramanian,[a] Prashant Sonar,[a] Jonathan Hobley,[a] Samarendra P. Singh,[b] Hiroyuki Matsuzaki,[c] Akihiro Furube[c] and Ryuzi Katoh[d]

We investigate the blend morphology and performance of bulk heterojunction organic photovoltaic devices comprising the donor polymer, pDPP-TNT (poly{3,6-dithiophene-2-yl-2,5-di(2-octyldodecyl)-pyrrolo[3,4-*c*]pyrrole-1,4-dione-*alt*-naphthalene}) and the fullerene acceptor, [70]PCBM ([6,6]-phenyl C71-butyric acid methyl ester). The blend morphology is heavily dependent upon the solvent system used in the fabrication of thin films. Thin films spin-coated from chloroform possess a cobblestone-like morphology, consisting of thick, round-shaped [70]PCBM-rich mounds separated by thin polymer-rich valleys. The size of the [70]PCBM domains is found to depend on the overall film thickness. Thin films spin-coated from a chloroform : dichlorobenzene mixed solvent system are smooth and consist of a network of pDPP-TNT nanofibers embedded in a [70]PCBM-rich matrix. Rinsing the films in hexane selectively removes [70]PCBM and allows for analysis of domain size and purity. It also provides a means for investigating exciton dissociation efficiency through relative photoluminescence yield measurements. Devices fabricated from chloroform solutions show much poorer performance than the devices fabricated from the mixed solvent system; this disparity in performance is seen to be more pronounced with increasing film thickness. The primary cause for the improved performance of devices fabricated from mixed solvents is attributed to the greater donor–acceptor interfacial area and resulting greater capacity for charge carrier generation.

Received 29th May 2013
Accepted 20th August 2013

DOI: 10.1039/c3ra42636j

www.rsc.org/advances

1. Introduction

Organic photovoltaics (OPV) have attracted considerable attention with the promise of large-scale, solution-based processing and the great extent to which the materials' optical and electronic properties can be tuned through organic synthesis and device fabrication. Reported power conversion efficiencies continue to rise and have already surpassed 10%.[1]

The production of photocurrent in OPV is generally described by three processes: the absorption of light which results in the formation of an excited state – the exciton, the dissociation of the exciton or bound electron–hole pair into free charge carriers, and the transport of charge carriers through the bulk of the active medium to the electrodes.[2] The relatively large exciton binding energy exhibited by organic semiconductors requires donor (D) and acceptor (A) materials to be employed in OPV devices, whereby the energy level offset between the D and A overcomes the binding energy, promoting charge transfer.[3] After photon absorption, the excited state exciton has to reach the D–A interface within its limited lifetime, (typical diffusion length of excitons are <10 nm) and to increase the likelihood of the exciton reaching a D–A interface, the D and A materials are often blended together within the active layer in a bulk heterojunction (BHJ) device architecture.[4] This blend should ideally provide both a large D–A interfacial area for charge generation as well as continuous pathways to the electrodes for efficient charge transport and collection. Understanding and controlling the BHJ morphology is of principle importance for device performance and a focus of concentrated research efforts.

The choice of solvent used during the fabrication of BHJ films has been shown to have a dramatic effect on the performance of devices employing a polyphenylene vinylene-based polymer donor and fullerene acceptor. Increased solubility of

[a]*Institute of Materials Research and Engineering, A*STAR, 3, Research Link, 117602, Singapore. E-mail: williamse@imre.a-star.edu.sg; goreliks@imre.a-star.edu.sg; Fax: +65 67741042; Tel: +65 68747992*

[b]*Shiv Nadar University, Village Chithera, Tehsil Dadri District, Gautam Budh Nagar, 203207, Uttar Pradesh, India*

[c]*National Institute of Advanced Industrial Science and Technology (AIST), Tsukuba, Japan*

[d]*Nihon University, Fukushima, Japan*

† Electronic supplementary Information (ESI) available. See DOI: 10.1039/c3ra42636j

the fullerene led to finer scale mixing, increased interaction between polymer chains and greater photocurrent production.[5] Slow drying of the BHJ active layer was shown to increase ordering and crystallinity of the polymer in polythiophene-based solar cells resulting in improved charge transport characteristics and increased photocurrent.[6] The incorporation of a high boiling point additive to the solution was also shown to allow for improved ordering of the polymer component and enhanced device performance. The guidelines for choosing an effective additive include: a preferential solubility for one component of the D–A system, and a significant difference in boiling point between the components of the solvent system.[7] Along similar lines, mixed solvent systems wherein solvents with different boiling points and preferential solubility for one solute have also been shown to affect morphology and improved performance.[8]

Diketopyrrolopyrrole (DPP)-based materials, both polymer and small molecule, have gained significant interest in recent years owing to the frequently displayed high charge carrier mobility values, around 1 $cm^2\ V^{-1}\ s^{-1}$,[9] and low optical band gap (well suited for absorption of solar radiation)[10] with solar cells showing power conversion efficiencies around 7%.[11] The film morphology of the active layer of solar cells utilizing DPP-based materials is often found to be influenced by the solvent system employed during fabrication; the incorporation of an additive or poor solvent frequently produces devices with greater power conversion efficiency.[8,11–16] This means of controlling the blend morphology makes DPP-based devices particularly attractive for studies which relate blend morphology to device performance.[17]

In this paper we investigate the thin film morphology of BHJ devices employing pDPP-TNT (poly{3,6-dithiophene-2-yl-2,5-di(2-octyldodecyl)-pyrrolo[3,4-*c*]pyrrole-1,4-dione-*alt*-naphthalene})[16] and [70]PCBM ([6,6]-phenyl C71-butyric acid methyl ester) (Scheme 1). The roles of solvent choice and active layer thickness on BHJ morphology and subsequent device performance are investigated in detail. Device performance was characterized with standard current–voltage response and Incident Photon-to-collected-electron Conversion Efficiency (IPCE) measurements. Active layer morphologies were determined using atomic force microscopy (AFM), transmission electron microscopy (TEM), and energy filtered transmission electron microscopy (EFTEM).

We find pDPP-TNT to be an interesting polymer to utilize in morphology studies for two primary reasons. The first being that it is particularly well-suited for mixed solvent systems, which require a poor solvent component. pDPP-TNT is insoluble in many organic solvents which are commonly used in OPV fabrication, such as toluene, chlorobenzene, and dichlorobenzene (ESI, Fig. S1†). Chloroform is the rare solvent that pDPP-TNT is soluble in. This insolubility in most solvents is quite different from other DPP-based polymers.[11] The second reason is that pDPP-TNT appears to be largely immiscible with the fullerene acceptor, as will be discussed in this paper. An ideal polymer:fullerene bulk heterojunction should generally have a domain structure in which the domains are pure, with good molecular packing to provide good charge transport properties. The donor and acceptor domains should also co-exist on a small length scale to provide a large interfacial area and efficient exciton dissociation.

The above mentioned characteristics of low solubility and immiscibility in fullerene make it possible to systematically alter the blend morphology. This enables us to investigate the correlation between the physical structure of the film and the photophysical and optoelectronic properties.

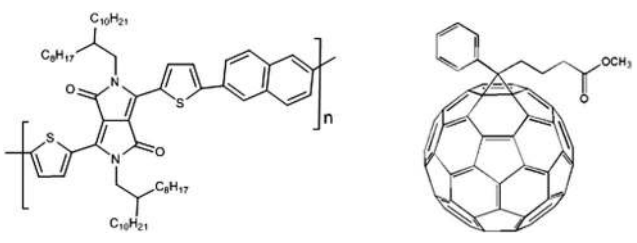

Scheme 1 Molecular structure of pDPP-TNT polymer and [70]PCBM used in this study.

2. Experimental

2.1. Materials

pDPP-TNT was synthesized in-house as described in previous work.[16] [70]PCBM was purchased from American Dye Source. Indium Tin Oxide (ITO)-coated glass was purchased from Kintec Company. PEDOT:PSS (Clevios P VP Al 4083) was purchased from Heraeus. Anhydrous chloroform (99.5% pure) and dichlorobenzene (99.0% pure) were purchased from Sigma Aldrich and Alfa Aesar, respectively.

2.2. Sample fabrication

Solutions were prepared by dissolving and stirring pDPP-TNT and [70]PCBM (weight ratios of 1 : 1, 1 : 2, and 1 : 3) in chloroform at 60 °C for several hours. The solution was split into two batches and *ortho*-dichlorobenzene (DCB) was added to one batch to constitute a ratio of 4 : 1 chloroform : DCB (additional chloroform was added to the other batch so as to maintain the same solute concentration); the solutions continued to stir at 60 °C for several more hours (typically overnight). Additionally, for the 1 : 2 blend ratio, the relative concentration of DCB in chloroform was varied (5%, 10%, 20%, 30%, 50%). The ITO coated glass (or glass in the case of AFM samples) was cleaned in subsequent ultrasonic baths of detergent, deionized water, acetone, methanol, and isopropanol for 10 minutes each and dried in an oven at 80 °C before being cleaned by UV-ozone for 10 minutes. PEDOT:PSS was spin-coated and the films were placed on a hot plate inside a nitrogen-filled glovebox at 140 °C for 10 minutes. The substrates and solutions were allowed to cool to room temperature before spin-coating inside the glovebox. Al cathodes were deposited on top of the active layer *via* thermal evaporation under vacuum, at a pressure less than 10^{-5} mbar through a shadow mask, defining device areas of 3 mm × 3 mm.

TEM samples were prepared by floating the active layer of the device off of the substrate in deionized water. The floating flakes of BHJ film were then lifted onto lacy carbon grids. This resulted in the flakes being suspended over holes in the lacy carbon; TEM characterization was performed at these locations with free-hanging film.

Samples for UV-vis measurements were fabricated on glass microscope slides in a similar way as devices.

Samples for variable angle spectroscopic ellipsometry were made by spin-coating solutions as described above on silicon wafers with a native oxide layer.

For the selective rinsing out of [70]PCBM from the BHJ films, samples were placed in a Petri dish and 4 mL of hexane was added, submerging the films. The solution was gently stirred, and after 10 minutes, the sample was removed and the solution was removed from the Petri dish and saved for UV-vis measurements. The rinsing was done inside a nitrogen-filled glovebox.

For photoluminescence (PL) measurements films of different thickness were spin-coated on glass substrates and encapsulated using soda-lime glass encapsulation caps and UV-curable epoxy, DELO-KATIOBOND LP655, inside the glove box. For each film thickness, two samples were spin-coated; one was then rinsed in hexane.

2.3. Sample characterization

OPV devices were characterized using IPCE and current density–voltage (*J–V*) response measurements, as previously described.[18] UV-vis absorption spectra were recorded using a UV-vis spectrophotometer (Shimadzu UV-2501PC). TEM imaging and elemental mapping was done with an FEI Titan TEM with a Schottky electron source, operated at 80 kV. A Gatan HR Tridiem EELS (electron energy loss spectroscopy) detector was used for EELS and energy-filtered imaging. The sulfur maps were obtained with the three-window method, where electrons from 20 eV energy windows were used to form an image of a $\sim 2 \times 2$ μm area at three slightly different energies: 138, 151 and 177 eV. The signal in each pixel of first two windows was extrapolated using a power-law fit, which was then subtracted from the EELS counts in the 177 eV window. The remaining background-subtracted signal from the 177 eV window shows the spatial distribution of sulfur, which has a core-loss signal (arising from the sulfur $L_{2,3}$ edge) around this energy. Each filtered image was acquired for 60 s, and spatial drift was corrected before processing the background signal.

AFM measurements were carried out using a Bruker Dimension Icon equipped with a NanoScope V controller. Silicon cantilevers from Nanosensors were used for intermittent contact (tapping) mode operation. AFM images were analyzed using a WSxM 5.0 develop 6.3 software (Nanotec Electronica S.L.).

Film thicknesses of devices and AFM-measured films were determined by scratching the films and measuring with a surface profilometer (KLA Tencor P-10).

Variable angle spectroscopic ellipsometry measurements were carried out using Woolam (WVASE-32) ellipsometer in the spectral range 300–1200 nm using three different angles of incidence: 65°, 70°, 75°. At first, measurements were performed in the spectral region, where the sample does not absorb (850–1200 nm). Film thickness was determined by fitting the data in this spectral region using the Cauchy model. The thickness value was fixed for point to point fitting of the experimental data for other wavelengths using only n and k as fitting parameters.[19]

For PL measurements the samples were positioned in the center of the integrating sphere (6 inch diameter, Labsphere) equipped with an Ocean Optics USB4000 CCD array spectrometer as a detector. PL was excited at 660 nm using a 60 mW cw diode laser (Coherent, Cube 660-100C). A 715 nm long pass filter was placed in front of the spectrometer entrance to suppress the signal from the excitation light. PL spectra and the absorptance of the laser radiation were measured using the procedure described by deMello *et al.*[20] To determine the relative PL yields, PL spectra of all films were normalized to their absorptance of the excitation laser radiation and the ratio of such normalized PL spectra of non-rinsed to corresponding rinsed films was calculated. Only the PL signal at wavelengths longer than 800 nm was taken into account because at shorter wavelengths the PL signal was strongly affected by self-absorption.

PL spectra of rinsed films spin-coated from chloroform as well as from the mixed solvent system normalized to their corresponding absorptance at the excitation wavelength are shown in ESI Fig. S2.† Similarly normalized PL spectrum of the neat pDPP-TNT film is shown as well.

3. Results and discussion

3.1. OPV performance

OPV devices were fabricated as described in the Experimental section from solutions of pDPP-TNT:[70]PCBM (various weight ratios), in both chloroform and chloroform : DCB. In general, devices employing a donor–acceptor ratio of 1 : 2 showed better performance than 1 : 1 and 1 : 3 ratios (ESI, Table S1†). Therefore, in this study, we focus on devices employing a donor–acceptor ratio of 1 : 2.

Devices with a 1 : 2 blend ratio with varying relative amounts of DCB in chloroform were fabricated as described in the Experimental section, and all devices showed similar improvements in photocurrent generation, as compared to devices fabricated from chloroform only (ESI, Fig. S3†). Given the similar performance, in this study we chose to focus on a single ratio of solvents, 4 : 1 chloroform : DCB. This is in line with many studies which also use a 4 : 1 ratio in the fabrication of DPP-based OPV devices.

OPV devices with a 1 : 2 weight ratio of pDPP-TNT:[70]PCBM were fabricated. Thicknesses of the resulting active layers were similar for both solvent systems, and around 110 nm. It was found that the performance of these devices varies greatly with the choice of solvent system. Fig. 1 shows IPCE spectra (top) and *J–V* curves (bottom) for devices in which the active layer was spin-coated from either chloroform or a mixed chloroform : DCB (4 : 1) solvent system. The key performance parameters are summarized in Table 1. The device fabricated from mixed solvents shows much higher performance than the

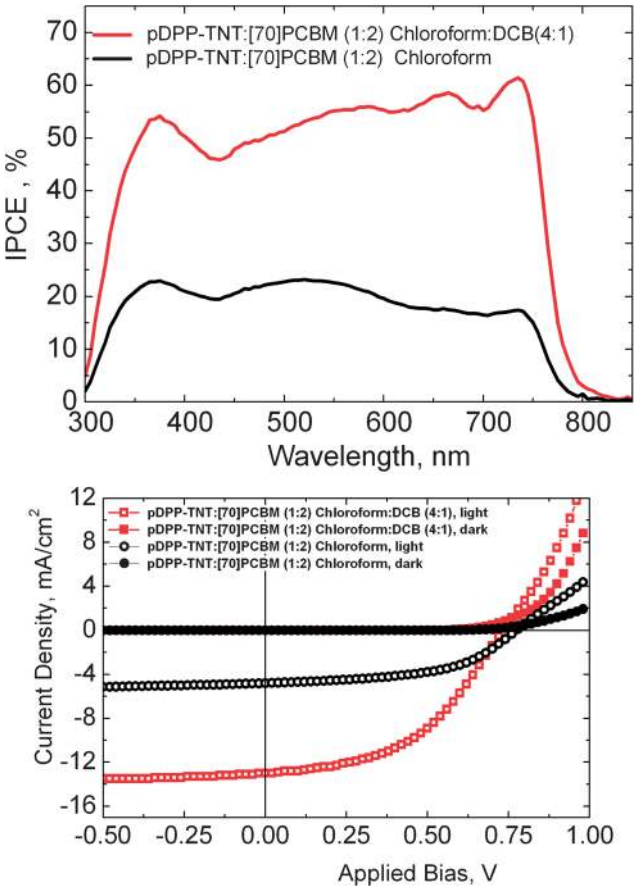

Fig. 1 IPCE spectra (top) and *J–V* curves (bottom) for devices with active layers spin-coated from chloroform only (black) and from chloroform : DCB (4 : 1) mixed solvent system (red).

device fabricated from chloroform. DCB has been shown to be a poor solvent for several DPP-based polymers[8,14] and pDPP-TNT shows very limited solubility in DCB at temperatures used during device processing (solutions were stirred at 60 °C for dissolution and spin-coated at room temperature). The difference in performance can most likely be attributed to the difference in blend morphology, with the film made from mixed solvents having a morphology that results in greater photocurrent production. Therefore, a systematic study of the solvent effect on film morphology and its relation to device performance was carried out *vide infra*.

3.2. AFM analysis

Fig. 2 shows AFM scans of BHJ films spin-coated from chloroform (top) and from mixed solvent system (bottom). The film spin-coated from chloroform shows large features in a "cobblestone"-like pattern with round, mound features of greater thickness separated by thinner valleys. Dimensions of the large features range from 200–500 nm laterally and are around 25 nm in height. Using a combination of AFM and TEM, such structures have been attributed to large domains of fullerene as was observed for PPV-based devices.[21] A finer structure showing smaller, needle-like structures can be seen in the valley regions. Typical dimensions of the needles appear to be around 60 nm in length. AFM images of neat pDPP-TNT films show similar characteristics (ESI, Fig. S4†) and it may be inferred that the valleys are polymer-rich regions. It is interesting to note that similar needles were observed in AFM images of BHJ films utilizing DPP-based oligomers[22,23] as well as other DPP-based polymers.[15,24] The film spin-coated from the mixed solvent system shows a distinctly different topography. The surface is, in general, much smoother. Some fine feature structure can be seen in addition to what appear to be small cracks in the film.

Relating the AFM images with the device data suggests the mixed solvent system may produce a greater mixing of donor and acceptor, generating greater photocurrent, while the morphology arising from the chloroform may consists of larger scale donor–acceptor phase segregation and provides less donor–acceptor interfacial area from which to generate charge carriers. However, whereas AFM analysis provides valuable information related to the film surface structure and can provide insight into the film morphology and potential growth mechanism(s), on its own it is not always well suited to specifically distinguish between donor and acceptor species in the blend. This is because it simply measures the differences in height, hardness and friction on the blend surface and does not give exact chemical information. Therefore, to relate specific features observed in AFM to donor and acceptor distributions we have complimented this AFM data with data obtained from TEM and EFTEM.

Table 1 Key OPV performance parameters for the devices fabricated from chloroform and mixed solvent system

	Chloroform	Mixed solvent
J_{sc}, mA cm^{-2}	4.8	13
V_{oc}, V	0.77	0.73
FF	52	47
PCE, %	1.9	4.5

3.3. TEM analysis

TEM was used to further investigate the morphology of the active layer. Fig. 3 shows bright field TEM (BFTEM) images of the blend film spin-coated from chloroform (top left) in which we can see large dark regions separated by narrower light regions in between. This is in good agreement with the AFM image where the valleys can be considered to correspond to the bright regions and the mounds correspond to the dark regions. The BFTEM image of the blend film spin-coated form mixed solvents (top right) shows a network of nanofibers, which were not evident in the AFM images. This suggests these nanofibers exist within the bulk of the film and are not simply surface features. The individual fibers typically appear to be around 15–20 nm in width. As the BFTEM image is a projection of the entire thickness of the film onto the image plane it is difficult to determine the orientation or absolute length of the fibers; observed lengths typically do not exceed 300 nm. The fibers appear lighter in color than most of the background which suggests that the fibers are less dense (less scattering) than the

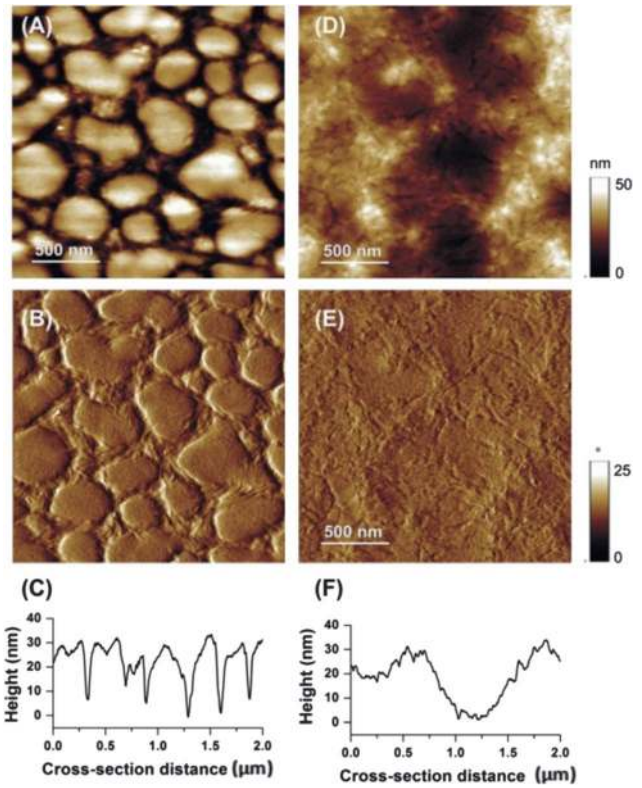

Fig. 2 AFM images of pDPP-TNT:[70]PCBM BHJ films spin-coated from chloroform only: (A–C) from chloroform : DCB (4 : 1) mixed solvent system (D–F). (A and D) – height images, (B and E) – phase images, (C and F) – height profiles.

surrounding matrix, suggesting a difference in chemical or structural composition.

EFTEM has been used to investigate phase segregation in BHJ films by distinguishing between the chemical composition of D and A materials.[25–27] In the case of pDPP-TNT:[70]PCBM blends, the spatial distribution of the polymer can be mapped as the polymer repeat unit contains two sulfur atoms (for every 64 carbon atoms) whereas the fullerene unit contains no sulfur (EELS spectra for neat pDPP-TNT and [70]PCBM films are provided in ESI, Fig. S5†).

In a BHJ film with a 1 : 2 ratio of polymer to fullerene we might expect, as an approximation, an additional 164 carbon atoms for every two sulfur atoms in the film (2 : 228). The sensitivity limit of EFTEM (around 0.1 atomic%) allows us to map the sulfur distributions but limits the extent to which the data can be quantitatively analyzed.

Fig. 3 contains the EFTEM sulfur maps of the film areas shown in the BFTEM images. The image of the film spin-coated from chloroform (bottom left) contains the same features as the corresponding BFTEM image. In this case the sulfur-rich regions (therefore polymer rich) in the EFTEM correspond to the bright regions in the BFTEM image. By analogy the dark regions in the BFTEM image can be assigned to fullerene-rich regions. Since the BFTEM images contain the same features as the AFM images we can further state that the valleys in the AFM image are polymer-rich and the mounds are fullerene-rich. The terms fullerene-rich and polymer-rich were deliberately chosen because, whereas we can state that the polymer-rich regions clearly contain sulfur, we cannot state that the fullerene-rich regions do not contain sulfur (and therefore polymer) with high confidence. Likewise, we cannot say that the polymer regions do not contain fullerene. Therefore, the domains may in fact only be partially de-mixed in reality. We state this because of the limitations of detection and quantification mentioned above.

The EFTEM image of the film spin-coated from the mixed solvent system (bottom right) shows that the nanofibers, which were seen as bright regions in the BFTEM image, are sulfur-rich and we can therefore conclude that these bright nanofibers contain significant amounts of polymer. It is difficult to say if the polymer forms fibers in the valleys of the chloroform cast film due to the lack of contrast with the background (the matrix is so sulfur-rich that spatial features do not stand out). Liu *et al.* have investigated the growth of BHJ films utilizing a DPP-based polymer and [70]PCBM from chloroform : DCB solutions. X-ray diffraction and X-ray scattering measurements during film drying suggest the polymer begins to crystallize as the chloroform evaporates and the DPP becomes less soluble in the remaining DCB. As the DPP continues to crystallize during film drying a crystalline fibril network is formed.[14]

3.4. Nanofibers

The growth of organic semiconductor nanofibers or nanowires has received considerable attention for a variety of optoelectronic and electronic applications. There is particular interest from the organic thin film transistor (OTFT) and OPV communities under the premise of improved charge carrier transport due to molecular ordering within the wire and as a means for forming beneficial charge transport pathways within a BHJ blend. Top down methods for forming nanowires, such as electrospinning have been well utilized for forming nanostructures in a variety of material systems.[15,28] Bottom up approaches to assembly that rely on intermolecular forces, such as π–π interactions, have been of particular interest to the organic semiconductor community. This is because the π–π stacking can lead to increased electrical conductivity. Poor solvent systems have been used to promote nanofiber growth in poly(3-hexylthiophene) (P3HT) for OPV applications. The aggregation of the polymer and the formation of the fibers was evidenced by the appearance of low energy absorption bands in the UV-vis absorption spectrum, indicative of π–π stacking.[29,30]

It has been shown that the polymer chains in P3HT nanofibers orient in a way such that the long axis of the chain lies across the width of the fiber and lamellar sheets stack by π–π interactions parallel to and along the length of the fiber.

The molecular weight of the pDPP-TNT used in this study corresponds to average chain lengths having roughly 50 repeat units. We estimate the length of an individual repeat unit to be approximately 1.5 nm, and hence the length of a perfectly straight and rigid chain would be around 75 nm. The nanofibers observed in BFTEM images range in width from 5–25 nm and are, on average, around 15 nm. Given the estimated pDPP-TNT chain length, it is improbable that the polymer chains lie in a straight, stretched configuration across the nanofiber width. We

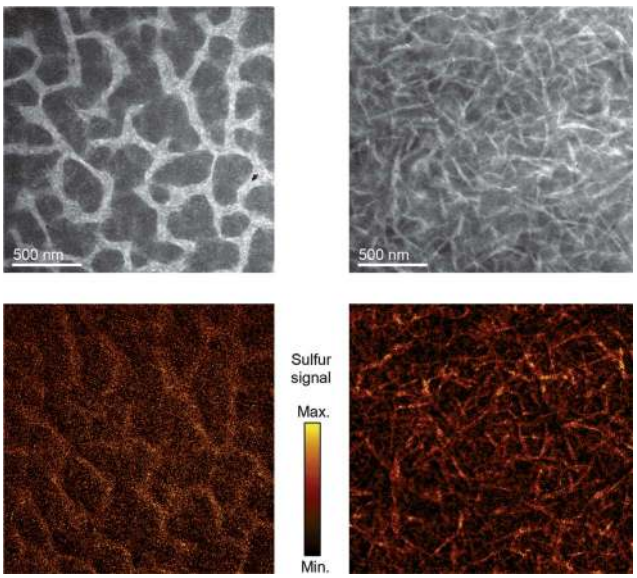

Fig. 3 Top: bright field TEM images of BHJ films spin-coated from chloroform (left) and from chloroform : DCB (4 : 1) mixed solvent system (right). Bottom: sulfur maps corresponding to the top images, obtained using energy filtered TEM.

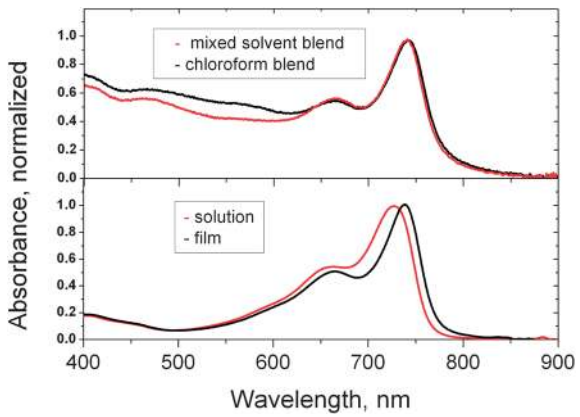

Fig. 4 Normalized absorption spectra of (top) BHJ films spin-coated from chloroform only (black) and from chloroform : DCB (4 : 1) mixed solvent system (red), (bottom) neat pDPP-TNT film (black) and pDPP-TNT diluted chloroform solution (red).

therefore infer that the polymer chain may adopt a coiled configuration or lie with the long axis largely along the length of the fiber.

Fig. 4 (top) shows the UV-vis absorption spectra of the BHJ films from chloroform and mixed solvents. The spectra are very similar and no additional low energy absorption can be identified for the mixed solvent film which is known to contain nanofibers. This suggests that either no additional π–π stacking occurs in the nanofiber as compared to the chloroform thin film or that the chloroform thin film contains nanofibers. Fig. 4 (bottom) shows the absorption spectra of pDPP-TNT in dilute solution and thin film. The relatively small shift in the peak position is of interest, in reference to well-studied organic semiconductors such as P3HT and PTCDA which show peak shifts of around 100 nm.[31] The small shift that we observe in the case of pDPP-TNT thin films can be attributed to losses in transmission due to high reflection in the spectral region around the absorption maximum. This large reflection is caused by the high absorption coefficient of the film and the consequent change in refractive index in the vicinity of the absorption maximum (as described by the Kramers–Kronig relation).

Some DPP-based polymers and many DPP-based small molecules exhibit a significant increase in the long wavelength region of the absorption spectrum of thin films, relative to dilute solutions, which could be attributed to π–π stacking.[8,32] However, it has been noted that several DPP-based polymers, even those demonstrating high charge carrier mobility, display only modest (less than 20 nm) red-shifts of the absorption peaks when going from solution to solid films. The fact that these shifts were small was attributed to the polymers already possessing a highly coplanar rigid chain conformation in solution, which was retained upon going to thin film as reported by Zhang *et al.*[17]

Conversely, DPP-TNT, the repeat unit and a model compound for pDPP-TNT, was studied by Lee *et al.* using density function theory calculations to investigate its backbone planarity. These authors determined torsional angles of 15° and 28° between the DPP–thiophene groups and the thiophene–naphthalene groups, respectively.[33] This suggests that the DPP unit is more conjugated to the thiophene unit than the naphthalene is to the thiophene and also raises questions regarding the coplanarity amongst repeat units within the entire pDPP-TNT chain. Lee *et al.* also carried out density function theory studies on repeat units for two of their polymers investigated by Zhang *et al.* and found them to be more planar than the DPP-TNT repeat unit.

Despite DPP-TNT being the least coplanar of the polymer repeat units discussed above, there is no significant change in the absorption spectrum of pDPP-TNT upon going from solution to thin film. In this respect we are in agreement with Zhang *et al.*; the planarity, and therefore the effective conjugation, of pDPP-TNT does not change upon going from solution to thin film. The observed spectra result from the intramolecular charge distribution and conjugation of the polymer, rather than intermolecular interactions. With no obvious optical signature of π–π interaction in solid samples, nor any change in the planarity due to packing factors, the driving force for nanofiber formation still remains unclear.

3.5. Influence of film thickness on morphology

To further investigate the mechanism of pDPP-TNT:[70]PCBM film formation and the resulting morphology, a range of films of different thickness were prepared by spin-coating from solutions with different concentrations. AFM images of the films are shown in Fig. 5. All of the films spin-coated from chloroform (top row) show the characteristic cobblestone-like pattern, discussed above, with the [70]PCBM domain sizes being smaller for thinner films. For the thinnest film, it can be seen that most of the [70]PCBM domains are round in shape. The average [70]-PCBM domain size increases with thickness although the

general morphology remains similar, except for the thickest film, for which the features are less defined. The shape of the domains and increase of their size with the film thickness are very similar in characteristic to previously reported blend morphologies formed by surface directed spinodal decomposition.[34–38] In cases of surface-directed spinodal decomposition involving a blend system, a difference in the surface energies of the blend components at the substrate surface and at the free surface induces a transient liquid bilayer (or multilayer) system to form. The layer interfaces are parallel to the surface of the substrate. This bilayer system can be destabilized by any interfacial instability forcing the blend components to phase separate laterally *via* liquid–liquid dewetting and form the domain structure. The size of the initially formed domains is dictated by the instability wavelength, which depends on the overall film thickness – the thicker the film the larger the wavelength.[34]

Additionally, domains can grow and coalesce until solidification is completed.[37] Surface-directed spinodal decomposition has been observed in spin-coating thin blend films from volatile solvents of: two immiscible or partially miscible polymers,[35–37,39,40] polymer and PCBM,[38,41] as well as small organic dye molecules and PCBM.[34] The films spin-coated from mixed solvent are much smoother than the chloroform counterparts and there is not much change with thickness (Fig. 5 bottom row). We assume the key factor for the mixed solvent to produce smoother films is the good solubility of the fullerene in DCB and concurrent poor solubility of pDPP-TNT in DCB. Additionally, DCB is much less volatile than chloroform and the film takes longer to dry and completely solidify. Therefore, as the chloroform evaporates and the solvent system becomes increasingly DCB-rich the polymer aggregates and assembles into nanofibers, while PCBM still remains in solution. Furthermore, the pDPP-TNT nanofibers may act as a network, trapping unincorporated polymer and the fullerene within the matrix of the film. This type of growth is in agreement with the description of Liu *et al.*[14]

3.6. Influence of film thickness on device performance

To investigate the influence of BHJ film thickness and the nanostructure feature sizes on device performance, solar cells were fabricated using similar procedure as the films described in Fig. 5. The *J*–*V* characteristics and IPCE spectra are shown in Fig. 6. The key performance parameters are summarized in Table 2. Two general trends can be identified. First, for both chloroform and mixed solvent devices (though slightly less clear in the case of chloroform) the relative contribution to photocurrent of the longer (>600 nm) wavelength region becomes more significant with increasing thickness. For thinner active layers the IPCE values below 600 nm are substantially greater than above 600 nm. For thicker active layers the IPCE values above and below 600 nm become comparable. We note that [70]PCBM absorbs most prominently below 600 nm while pDPP-TNT absorbs most significantly above 600 nm. Second, the difference in device performance between chloroform and mixed solvent devices is less for thinner active layers. The difference in performance becomes more pronounced as the device becomes thicker (devices around 40 nm thick have very similar J_{sc}, while for ~110 nm thick the mixed solvent device shows a J_{sc} around 3–4 times that of the chloroform device).

We considered optical absorptance saturation to be the primary cause for the dependence of IPCE spectral shape on thickness. To further investigate, we calculated the total absorptance (fraction of the incident light which is absorbed) of the thin film stack using the commercial software program SETFOS from FLUXiM. To obtain real and imaginary parts of the refractive index (*n* and *k*) of the blend film, variable angle spectroscopic ellipsometry was used (ESI, Fig. S6†). The obtained *n* and *k* values were used to model the absorptance of a thin film stack consisting of glass/ITO (125 nm)/PEDOT:PSS(40 nm)/BHJ (varied thickness)/Al (150 nm). The default values from the software were used for optical parameters of all materials other than the BHJ active layer. The roughness of the film surface from chloroform was not accounted for. The simulated absorptance spectra for the

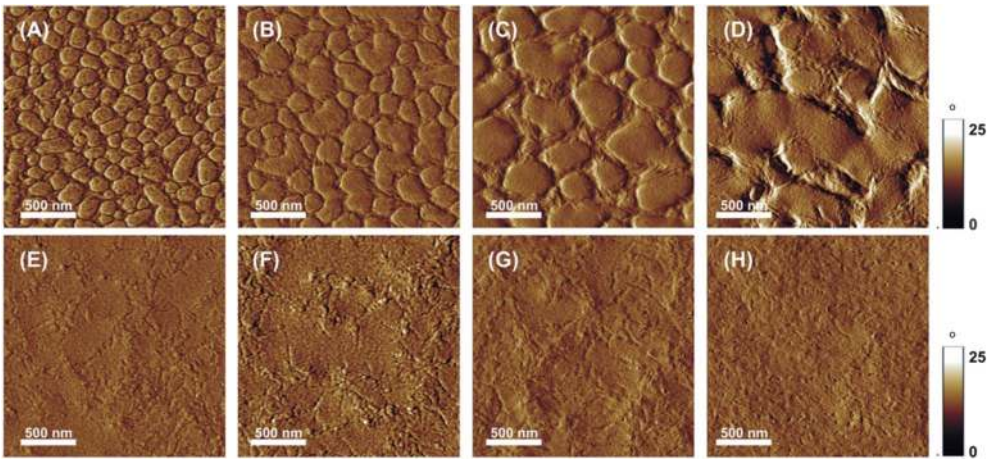

Fig. 5 AFM phase images for pDPP-TNT:[70]PCBM BHJ films with different thicknesses spin-coated from solutions with different concentrations. (A–D) Films spin-coated from chloroform only, (E–H) films spin-coated from chloroform : DCB (4 : 1) mixed solvent system. Initial solution concentrations and resulting film approximate thicknesses accordingly: (A) 2.5 mg mL^{-1}, 15 nm; (B) 4.5 mg mL^{-1}, 35 nm; (C) 9 mg mL^{-1}, 50 nm; (D) 15 mg mL^{-1}, 120 nm; (E) 4.5 mg mL^{-1}, 20 nm; (F) 6 mg mL^{-1}, 40 nm; (G) 9 mg mL^{-1}, 50 nm, (H) 15 mg mL^{-1}, 130 nm.

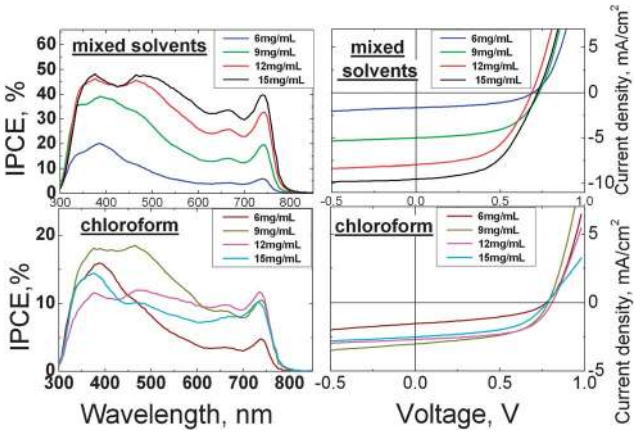

Fig. 6 IPCE spectra and *J–V* curves for devices of different thicknesses fabricated from chloroform only (bottom) and from chloroform : DCB (4 : 1) mixed solvent system (top). Device thickness was varied by changing the initial solution concentration. See Table 1 for performance parameters.

thin films stacks with BHJ layer thicknesses of: 40 nm, 60 nm, 80 nm, 100 nm and 120 nm can be seen in Fig. 7. The absorptance in the long wavelength region of the spectrum increases with increasing thickness, in qualitative agreement with the increased contribution to photocurrent in the long wavelength region of the experimental IPCE spectra.

For thicknesses greater than 60 nm, it can be seen that, the absorptance is nearly completely saturated throughout the spectrum.

3.7. The relationships between film thickness, domain size, interfacial area and exciton quenching

By rinsing BHJ films in hexane it was possible to selectively remove [70]PCBM from the blend, because the fullerene is soluble in the solvent and pDPP-TNT is not. BHJ films of varying thickness were rinsed which enabled us to more clearly define the spatial distribution of the polymer domains. Additionally it allowed us to evaluate the purity of the domains. Furthermore, by comparison of the photoluminescence (PL) of rinsed and unrinsed films, it was possible to evaluate the extent of fluorescence quenching and hence exciton quenching, in the blend films.

To evaluate the purity of the domains, the UV-vis spectra of both the hexane solutions used in rinsing and the rinsed thin films spin-coated from chloroform were measured. Typical spectra of the films after rinsing are shown in ESI Fig. S7.† The spectra of the rinsed films do not show any spectral characteristics of the [70]PCBM, suggesting it had all been rinsed away. Similarly, the spectra of the hexane rinse solutions (ESI, Fig. S8†) do not show any characteristics of pDPP-TNT absorption, indicating that no measureable amount of colloidal pDPP-TNT had been rinsed out of the film. From this, we ascertain that the domains contain pure components.

Similar to the case of chloroform films, the UV-vis spectra of the rinsed mixed solvent films had no features of fullerene absorption, and the hexane solutions used in rinsing do not show any features associated with pDPP-TNT absorption (ESI, Fig. S7 and S8†). Once again, this indicates that the domains contain pure components. The fact that no colloidal pDPP-TNT was found in the rinse suggests that the nanofibers seen in the TEM image are not isolated and rather exist in an interconnected network. Additionally, if the nanofibers had been isolated an observable decreases in the strength of the absorbance in the UV-vis spectrum of the film would be expected as such fibers would be washed out with the fullerene.

AFM images of the rinsed blend films spin-coated from chloroform and mixed solvents are shown in Fig. 8. The films spin-coated from chloroform have a well defined morphology with many holes where the [70]PCBM had been rinsed away, creating a continuous network of pDPP-TNT ridges. The area percentage (footprint) of the holes and the total perimeter of the holes were determined using image analysis software, and the resultant average hole radius, assuming circularly shaped holes was calculated. These parameters are summarized in Table 3. The average hole radius increases with film thickness from about 50 nm for 3 mg mL^{-1} film to about 140 nm for 15 mg mL^{-1} film, and the area percent of the hole ([70]PCBM) is around 50% for all thicknesses. Furthermore, using this area percent of the ([70]PCBM), we calculate a complimentary area percentage of pDPP-TNT and a volume fraction of the pDPP-TNT that is within 10 nm (Table 3) (a rule-of-thumb exciton diffusion length) of the domain interface, by multiplying the perimeter value by 10 nm.

The AFM images of rinsed mixed solvent films appear similar to the unrinsed films except that they are rougher.

OPV devices of different thickness showed different performance. The performance is the combined result of the efficiencies of absorption, exciton dissociation and charge transport and collection. To further complete our understanding of charge generation, PL studies were employed to gauge the efficiency of exciton dissociation for different film thicknesses and morphologies.

The efficiency of quenching excitons that were generated in pDPP-TNT was determined by measuring the absorptance and PL spectra of the films before and after rinsing using an excitation wavelength of 660 nm at which the [70]PCBM absorption is expected to be small and hence its contribution to PL signal was neglected. The relative PL yields of films fabricated from chloroform and mixed solvents are shown in Fig. 9, bottom.

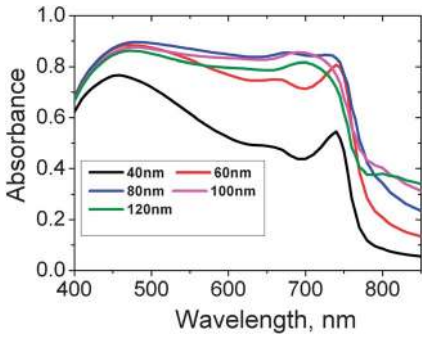

Fig. 7 Absorptance spectra for the thin film stacks corresponding to the device structure with different thickness of active layer simulated using SETFOS software. Real and imaginary parts of refractive index, *n* and *k*, were obtained using ellipsometry (see ESI, Fig. S4†).

The relative PL yield was calculated as a ratio of PL signals before and after rinsing, scaled to the corresponding film absorptance at the excitation wavelength.

It can be seen in Fig. 9, top (PL yield of rinsed film relative to neat pDPP-TNT film), that all rinsed films had a PL yield similar to that of a neat film of pDPP-TNT, which further confirms that there is not a significant amount of [70]PCBM remaining in the rinsed films. For all film thicknesses, the blends spin-coated from mixed solvent show a lower relative PL yield than chloroform films, suggesting a roughly twofold enhancement in exciton dissociation efficiency.

This implies that enhanced exciton dissociation plays a significant role in generating the larger photocurrents displayed by mixed solvent devices. This enhanced dissociation can be attributed to the smaller domain sizes of pDPP-TNT nanofibers in mixed solvent films as compared to the domain sizes in the chloroform films.

Given the observed purity of the domains, all exciton quenching and dissociation must occur at the interface between the donor and acceptor domains. It is therefore of interest to estimate the interfacial area and from this, the volume fraction of the domains which lie within an exciton diffusion length of the interface in the different films. This can then be compared with measured PL yields.

For the chloroform films, we consider the morphology to be approximated by isolated cylindrical pillars of [70]PCBM surrounded by continuous phase of pDPP-TNT as can be seen in Fig. 5 and 8.

For simplicity, we consider, a simple model consisting of just a single cylinder of [70]PCBM with a radius of r, surrounded by a cylindrical shell of pDPP-TNT with outer radius R, the areas of the inner cylinder and outer shell being equal. Given a 50% area coverage of the fullerene cylinders, and since.

$$A = \pi r^2,$$

$$R = \sqrt{2}r.$$

We further consider, as an upper limit, that all excitons created within 10 nm of donor–acceptor interface will be quenched. Thus, the volume fraction of pDPP-TNT that will be quenched as a function of r can be expressed as,

$$h(\pi(r + 10\ \text{nm})^2 - \pi r^2)/h\pi(R^2 - r^2),$$

for $R - r > 10$ nm, where h is the height of the interface between the inner cylinder and outer shell. This expression is plotted as a function of r in Fig. 10. For radii larger than 75 nm, there is no significant change in the percent of quenched polymer (30% at 70 nm to 15% at 150 nm), and only below a radius of 45 nm, is the polymer substantially (>50%) quenched.

Fig. 10 also shows the estimated quenched volume fraction of pDPP-TNT for the different film thicknesses and domain sizes of films studied here. It may be expected that thinner films, and smaller domains ($r \sim 50$ nm), would show relatively greater quenching efficiency (35% volume fraction quenched) than thicker films with larger domains ($r \sim 150$ nm, 15% volume fraction quenched).

However, all the domain sizes studied here are in a regime where $r > 50$ nm and the extent of exciton quenching is not expected to vary greatly.

For mixed solvent films, the film morphology can again be approximated as a series of cylinders within a matrix, however the cylinders are made up of pDPP-TNT (the observed nanofibers) and the matrix is fullerene. The cylinders are substantially longer than the film thickness and have a radius of ~7 nm. We did not observe a significant change in the nanofiber diameter for films of different thickness (ESI, Fig. S9†). According to the simple model, a cylinder with radius less than 10 nm should allow for complete exciton quenching.

From these quenched volume fraction estimations, the PL yield for chloroform films is expected to vary from 0.65 to 0.85 for the fabricated films, from thinnest to thickest. Measured relative PL yields for these films are about 0.7 for thinner films, which is in good agreement with the estimations, but about 0.4 for the

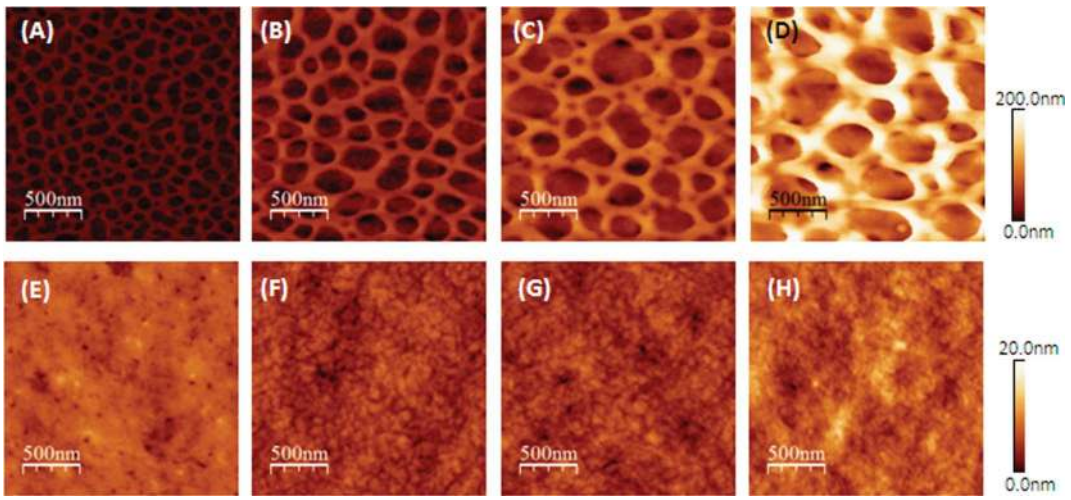

Fig. 8 AFM height images of films rinsed in hexane. (A–D) Rinsed films spin-coated from chloroform only, (E–H) rinsed films spin-coated from chloroform : DCB (4 : 1) mixed solvent system. Initial solution concentrations: (A) 3 mg mL^{-1}; (B) 6 mg mL^{-1}; (C) 9 mg mL^{-1}; (D) 15 mg mL^{-1}; (E) 3 mg mL^{-1}; (F) 6 mg mL^{-1}; (G) 9 mg mL^{-1}; (H) 15 mg mL^{-1}.

Table 2 Key performance parameters of the devices fabricated from chloroform and mixed solvents with different thickness of active layer

	6 mg mL^{-1} chloroform	9 mg mL^{-1} chloroform	12 mg mL^{-1} chloroform	15 mg mL^{-1} chloroform	6 mg mL^{-1} mix solvent	9 mg mL^{-1} mix solvent	12 mg mL^{-1} mix solvent	15 mg mL^{-1} mix solvent
Thickness, nm	40	50	90	120	40	50	90	130
J_{sc}, mA cm^{-2}	1.53	3.02	2.7	2.51	1.65	5.01	7.96	9.55
V_{oc}, V	0.77	0.78	0.81	0.76	0.69	0.73	0.68	0.72
FF	43	52	57	52	47	56	53	53
PCE	0.51	1.2	1.2	1	0.54	2.1	2.9	3.6

Table 3 Total hole footprint area fraction and total hole perimeter calculated for 5 μm × 5 μm AFM images of rinsed chloroform films using WSxM software, hole average radius, estimated as 2 × area/perimeter, as well as the footprint area of pDPP-TNT, estimated as 100% – hole area, and volume fraction of pDPP-TNT within 10 nm of D–A interface estimated as perimeter × 10 nm/area (pDPP-TNT)

Solution concentration used to fabricate film, [mg mL^{-1}]	Area % of holes ([70]PCBM)	Total perimeter of holes, [μm]	Average hole radius, [nm]	Area % of pDPP-TNT (100-area of holes)	Volume fraction of pDPP-TNT within 10 nm of domain interface
15	50	180	140	50	0.14
12	52	190	130	48	0.16
9	55	230	110	45	0.20
6	50	270	90	50	0.22
4.5	45	320	70	55	0.23
3	47	450	50	53	0.34

thickest film, which is significantly lower than expected from the above estimations. This discrepancy will be addressed later. For mixed solvent films, from the nanofiber diameter, the PL yield is expected to be 0%, while the measured PL yield is around 30–40%. This is significantly more than expected for such small domains and means that not all of the excitons generated in the nanofiber could be quenched. This could be because the real diffusion length is less than the diameter of the nanofiber. It may also be because excitons can travel along the long axis of the nanofiber and not encounter a donor–acceptor interface within their lifetime. We note that there may be a slight decrease in PL yield for thicker films, but in general, the PL yields are similar for all thicknesses, unlike the case for blends spin-coated from chloroform. This anomaly will be addressed next.

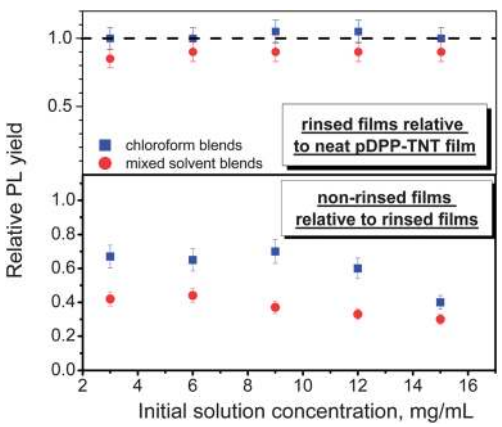

Fig. 9 Bottom: PL yields of blend films spin-coated from chloroform (blue squares) and mixed solvent system (red circles) relative to corresponding rinsed films. Top: PL yield of corresponding rinsed films relative to a neat pDPP-TNT film.

The variation of PL yields with domain size in blends spin-coated from chloroform (Fig. 9) cannot be explained by the simple model described above. In fact, it would be expected that the larger domain sizes investigated should have PL yields that are higher than for the films with smaller domain sizes. Given that the PL yields of all the rinsed films are similar and in agreement with neat polymer, we consider the apparently lower relative yield in the thicker blend films to be experimentally significant. However, we caution that this may arise from unquantifiable factors in the assumptions of the calculation. For example, it was assumed that the [70]PCBM absorbance in all of the films was zero. However [70]PCBM has a long absorption tail into the red region of the spectrum that lays beneath part of the pDPP-TNT spectrum. This tail can become extended further into the red if the [70]PCBM domains are more crystalline. If the [70]PCBM absorption increased, the calculated PL yield would decrease, even with the same fluorescence efficiency of the pDPP-TNT, due to the over-estimation of absorption in pDPP-TNT. For the thickest film from chloroform, the overestimation in absorption would be ~40% of the total absorptance at the excitation wavelength. Since thicker films have more time to form, they can become more ordered than their thinner counterparts and this may explain the anomaly. As an example of such behavior a series of poly(methyl methacrylate) (PMMA):[70]PCBM (1 : 2 by wt) films with varying thickness were spin-coated on glass substrates. The UV-vis spectra of these films clearly show the long wavelength tail of the [70]PCBM absorption increases with film thickness and become significantly greater than for that of a neat film of [70]PCBM (ESI, Fig. S10†). Other factors could also be present; however, we conclude by saying that the apparently lower yields are experimentally significant, but the mechanistic interpretation of this must be taken with caution. This, however, does not alter the conclusions for the comparison

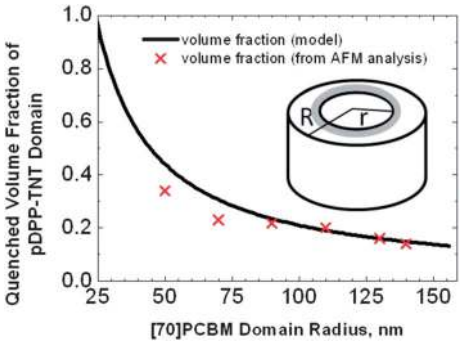

Fig. 10 Solid black line: quenched volume fraction of pDPP-TNT calculated using a model described in the text. Red crosses – results of AFM analysis from Table 3 column 6. 100% quenching efficiency within 10 nm of D–A interface was assumed.

between blends made from the different solvents, since for every thickness the reduction of PL yield for the blends made from mixed solvents was consistently lower than that for the blends made from chloroform.

The contribution to photocurrent from absorption in fullerene materials in OPV blends is well documented.[42] In blend systems where the absorption spectra of the donor polymer and the fullerene acceptor overlaps, significant absorption by the fullerene could influence device performance if certain conditions are realized. If the ratio of fullerene domain size to exciton diffusion length is larger than the ratio of domain size to exciton diffusion length in the polymer, a relative increase in absorption in the fullerene and corresponding decrease of absorption in the polymer would result in less photocurrent being generated in the device. Exciton diffusion lengths in [60]PCBM have been estimated to be around 5 nm,[43] which is shorter than in many polymers, for example poly(3-hexylthiophene) (P3HT), in which diffusion lengths have been determined to be around 30 nm.[44] Though we note that blends of [60]PCBM and P3HT are understood to mix on fine length scales. Additionally, if the energy level offsets between donor and acceptor created a scenario where exciton dissociation efficiency was more (or less) favourable after absorption in one of the blend components, as compared to the other,[45] a change in the relative amount of absorption in the donor and acceptor species would change the extent of photocurrent generation in the device.

Returning our attention to device performance, the photocurrent generation for chloroform devices increases with a slight increase of thickness (active layer thickness $\sim$ 50 nm) but then plateaus, or even drops slightly for thicker active layers. The larger domain sizes in the thicker films are expected to provide only a slight decrease in the relative volume fraction of donor or acceptor material near the interface, and thus a similar extent of exciton dissociation efficiency. Additionally, although the increased thickness might be expected to provide greater absorption and the potential for greater photocurrent generation, the thin film model of absorptance suggests that optical absorption is close to saturation for a film thickness greater than 60 nm. The lack of an increase in generated photocurrent with increasing thickness is quite consistent with the absorptance and morphology of the blends.

On the other hand, for devices made from mixed solvents there is an increase in generated photocurrent with increasing film thickness, which by analogy, should be caused by some additional effect, other than simply an increase in absorbance. Furthermore, the increased photocurrent should not be due solely to increased exciton dissociation efficiency, given the small decrease observed in the PL yield with thickness of blends made from mixed solvent. While we note that the FFs are similar for all the devices, changes in morphology with thickness may influence the charge carrier recombination properties, wherein thicker devices undergo less recombination and produce greater photocurrent.

4. Conclusion

We have investigated BHJ OPV devices made from pDPP-TNT:[70]PCBM, a system that shows dramatically improved photocurrent generation when the active layer is spin-coated from a mixed chloroform : DCB (4 : 1) solvent system as compared to simply chloroform. Morphology was analyzed and correlated with device performance. Films from chloroform consist of fullerene-rich mounds with surrounding polymer-rich valleys. Films from mixed solvents consist of polymer nanofibers embedded throughout a fullerene-rich matrix. The influence of film thickness (ranging from $\sim$40 to $\sim$130 nm) on morphology and device performance was studied. The typical fullerene domain size in chloroform films was dependent on film thickness; the typical domain size increased with film thickness. The performance of chloroform devices did not substantially increase with increased thickness. Despite the domain size increasing with film thickness, the quenchable volume fraction near the donor–acceptor interface did not significantly increase, because the domain sizes were all much greater than the exciton diffusion length. Furthermore, absorption saturation is expected for films thicker than 60 nm. Significantly more photocurrent was generated from mixed solvent devices with increasing thickness. The shape of the absorptance spectra defined the relative shape of the IPCE spectra. The performance of thin chloroform devices was comparable to thin mixed solvent devices while the performance of thick mixed solvent devices was far greater than thick chloroform devices. The enhanced performance upon incorporating the mixed solvent is largely attributed to the D–A interfacial area available in the given film morphology. Thick chloroform films, with large fullerene domains, have a limited D–A interfacial area from which to generate charge carriers. The extensive network of nanofibers present in thick films made from mixed solvents provides a large D–A interfacial area which benefits the generation of photocurrent, as validated by the PL yield measurements.

Experiments in which the [70]PCBM was selectively removed by rinsing in hexane gave a two-fold benefit. Firstly, they allowed us to estimate that the individual phase domains were substantially immiscible in each other. Secondly it enabled the evaluation of relative PL yields, whilst maintaining the pDPP-TNT morphology. The relative PL yield measurements, along with UV-vis measurements of thin films with varying thickness suggest an increasing contribution to absorption from

[70]PCBM; this could have implications on photocurrent generation in certain BHJ systems and morphologies.

Acknowledgements

This work was funded by the A*STAR-JST Strategic International Cooperative Programme (1st Joint Grant Call – project number 1021630071). Additionally, authors E.L.W. and P.S. would like to acknowledge the Visiting Investigatorship Programme (VIP), project number 0721100037, of the Agency for Science, Technology and Research (A*STAR), Republic of Singapore for support.

References

1 M. A. Green, K. Emery, Y. Hishikawa, W. Warta and E. D. Dunlop, *Prog. Photovoltaics*, 2012, **20**, 606.
2 C. J. Brabec, N. S. Sariciftci and J. C. Hummelen, *Adv. Funct. Mater.*, 2001, **11**, 15.
3 B. P. E. Shaw, A. Ruseckas and I. D. W. Samuel, *Adv. Mater.*, 2008, **20**, 3516.
4 N. S. Sariciftci, L. Smilowitz, A. J. Heeger and F. Wudl, *Science*, 1992, **258**, 1474.
5 S. E. Shaheen, C. J. Brabec, N. S. Sariciftci, F. Padinger, T. Fromherz and J. C. Hummelen, *Appl. Phys. Lett.*, 2001, **78**, 841.
6 B. C. Thompson and J. M. J. Frechet, *Angew. Chem., Int. Ed.*, 2008, **47**, 58.
7 J. K. Lee, W. L. Ma, C. J. Brabec, J. Yuen, J. S. Moon, J. Y. Kim, K. Lee, G. C. Bazan and A. J. Heeger, *J. Am. Chem. Soc.*, 2008, **130**, 3619.
8 M. M. Wienk, M. Turbiez, J. Gilot and R. A. J. Janssen, *Adv. Mater.*, 2008, **20**, 2556.
9 Y. N. Li, S. P. Singh and P. Sonar, *Adv. Mater.*, 2010, **22**, 4862.
10 C. B. Nielsen, M. Turbiez and I. McCulloch, *Adv. Mater.*, 2013, **25**, 1859.
11 L. Ye, S. Q. Zhang, W. Ma, B. H. Fan, X. Guo, Y. Huang, H. Ade and J. H. Hou, *Adv. Mater.*, 2012, **24**, 6335.
12 R. B. Aich, Y. P. Zou, M. Leclerc and Y. Tao, *Org. Electron.*, 2010, **11**, 1053.
13 J. C. Bijleveld, B. P. Karsten, S. G. J. Mathijssen, M. M. Wienk, D. M. de Leeuw and R. A. J. Janssen, *J. Mater. Chem.*, 2011, **21**, 1600.
14 F. Liu, Y. Gu, C. Wang, W. Zhao, D. Chen, A. L. Briseno and T. P. Russell, *Adv. Mater.*, 2012, **24**, 3947.
15 C. H. Woo, P. M. Beaujuge, T. W. Holcombe, O. P. Lee and J. M. J. Frechet, *J. Am. Chem. Soc.*, 2010, **132**, 15547.
16 P. Sonar, S. P. Singh, Y. N. Li, Z. E. Ooi, T. J. Ha, I. Wong, M. S. Soh and A. Dodabalapur, *Energy Environ. Sci.*, 2011, **4**, 2288.
17 X. R. Zhang, L. J. Richter, D. M. DeLongchamp, R. J. Kline, M. R. Hammond, I. McCulloch, M. Heeney, R. S. Ashraf, J. N. Smith, T. D. Anthopoulos, B. Schroeder, Y. H. Geerts, D. A. Fischer and M. F. Toney, *J. Am. Chem. Soc.*, 2011, **133**, 15073.
18 P. Sonar, E. L. Williams, S. P. Singh and A. Dodabalapur, *J. Mater. Chem.*, 2011, **21**, 10532.
19 W. A. McGahan, B. Johs and J. A. Woolam, *Thin Solid Films*, 1993, **234**, 443.
20 J. C. deMello, H. F. Wittmann and R. H. Friend, *Adv. Mater.*, 1997, **9**, 230.
21 H. Hoppe, M. Niggemann, C. Winder, J. Kraut, R. Hiesgen, A. Hinsch, D. Meissner and N. S. Sariciftci, *Adv. Funct. Mater.*, 2004, **14**, 1005.
22 A. B. Tamayo, B. Walker and T. Q. Nguyen, *J. Phys. Chem. C*, 2008, **112**, 11545.
23 A. B. Tamayo, X. D. Dang, B. Walker, J. Seo, T. Kent and T. Q. Nguyen, *Appl. Phys. Lett.*, 2009, **94**, 103301.
24 B. C. Thompson and J. M. J. Frechet, *Angew. Chem., Int. Ed.*, 2008, **47**, 58.
25 L. F. Drummy, R. J. Davis, D. L. Moore, M. Durstock, R. A. Vaia and J. W. P. Hsu, *Chem. Mater.*, 2011, **23**, 907.
26 D. R. Kozub, K. Vakhshouri, L. M. Orme, C. Wang, A. Hexemer and E. D. Gomez, *Macromolecules*, 2011, **44**, 5722.
27 M. Pfannmoller, H. Flugge, G. Benner, I. Wacker, C. Sommer, M. Hanselmann, S. Schmale, H. Schmidt, F. A. Hamprecht, T. Rabe, W. Kowalsky and R. R. Schroder, *Nano Lett.*, 2011, **11**, 3099.
28 A. L. Briseno, S. C. B. Mannsfeld, S. A. Jenekhe, Z. Bao and Y. Xia, *Mater. Today*, 2008, **11**, 38.
29 S. Berson, R. De Bettignies, S. Bailly and S. Guillerez, *Adv. Funct. Mater.*, 2007, **17**, 1377.
30 J. S. Kim, J. H. Lee, J. H. Park, C. Shim, M. Sim and K. Cho, *Adv. Funct. Mater.*, 2011, **21**, 480.
31 T. A. Chen, X. M. Wu and R. D. Rieke, *J. Am. Chem. Soc.*, 1995, **117**, 233.
32 B. Walker, A. B. Tamayo, X. D. Dang, P. Zalar, J. H. Seo, A. Garcia, M. Tantiwiwat and T. Q. Nguyen, *Adv. Funct. Mater.*, 2009, **19**, 1.
33 H.-S. Lee, J. S. Lee, S. Cho, H. Kim, K.-W. Kwak, Y. Yoon, S. K. Son, H. Kim, M. J. Ko, D.-K. Lee, J. Y. Kim, S. Park, D. H. Choi, S. Y. Oh, J. H. Cho and B. S. Kim, *J. Phys. Chem. C*, 2012, **116**, 26204.
34 J. Heier, J. Groenewold, S. Huber, F. Nuesch and R. Hany, *Langmuir*, 2008, **24**, 7316.
35 S. Heriot and R. A. L. Jones, *Nat. Mater.*, 2005, **4**, 782.
36 P. C. Jukes, S. Heriot, J. S. Sharp and R. A. L. Jones, *Macromolecules*, 2005, **38**, 2030.
37 S. Walheim, M. Böltau, J. Mlynek, G. Krausch and U. Steiner, *Macromolecules*, 1997, **30**, 4995.
38 S. Nilsson, A. Bernasik, A. Budkowski and E. Moons, *Macromolecules*, 2007, **40**, 8291.
39 E. Kim, G. Krausch and E. J. Kramer, *Macromolecules*, 1994, **27**, 5927.
40 M. Geoghegan, R. A. L. Jones and A. S. Clough, *J. Chem. Phys.*, 1995, **103**, 2719.
41 Y. Vaynzof, D. Kabra, L. H. Zhao, L. L. Chua, U. Steiner and R. H. Friend, *ACS Nano*, 2011, **5**, 329.
42 N. C. Nicolaidis, B. S. Routley, J. L. Holdsworth, W. J. Belcher, X. J. Zhou and P. C. Dastoor, *J. Phys. Chem. C*, 2011, **115**, 7801.
43 S. Cook, A. Furube, R. Katoh and L. Y. Han, *Chem. Phys. Lett.*, 2009, **478**, 33.
44 S. Cook, L. Y. Han, A. Furube and R. Katoh, *J. Phys. Chem. C*, 2010, **114**, 10962.
45 T. J. K. Brenner, Z. Li and C. R. McNeill, *J. Phys. Chem. C*, 2011, **115**, 22075.

